Dynamics of charged particle motion in the vicinity of three dimensional magnetic null points: Energization and chaos

Andrew Gascoyne

Citation: Physics of Plasmas (1994-present) **22**, 032907 (2015); doi: 10.1063/1.4916402
View online: http://dx.doi.org/10.1063/1.4916402
View Table of Contents: http://scitation.aip.org/content/aip/journal/pop/22/3?ver=pdfcov
Published by the AIP Publishing

Dynamics of charged particle motion in the vicinity of three dimensional magnetic null points: Energization and chaos

Andrew Gascoyne[a)]
School of Mathematics and Statistics, University of Sheffield, Hicks Building, Hounsfield Road, Sheffield S3 7RH, United Kingdom

(Received 27 January 2015; accepted 16 March 2015; published online 27 March 2015)

Using a full orbit test particle approach, we analyse the motion of a single proton in the vicinity of magnetic null point configurations which are solutions to the kinematic, steady state, resistive magnetohydrodynamics equations. We consider two magnetic configurations, namely, the sheared and torsional spine reconnection regimes [E. R. Priest and D. I. Pontin, Phys. Plasmas **16**, 122101 (2009); P. Wyper and R. Jain, Phys. Plasmas **17**, 092902 (2010)]; each produce an associated electric field and thus the possibility of accelerating charged particles to high energy levels, i.e., $>$ MeV, as observed in solar flares [R. P. Lin, Space Sci. Rev. **124**, 233 (2006)]. The particle's energy gain is strongly dependent on the location of injection and is characterised by the angle of approach β, with optimum angle of approach β_{opt} as the value of β which produces the maximum energy gain. We examine the topological features of each regime and analyse the effect on the energy gain of the proton. We also calculate the complete Lyapunov spectrum for the considered dynamical systems in order to correctly quantify the chaotic nature of the particle orbits. We find that the sheared model is a good candidate for the acceleration of particles, and for increased shear, we expect a larger population to be accelerated to higher energy levels. In the strong electric field regime ($E_0 = 1500$ V/m), the torsional model produces chaotic particle orbits quantified by the calculation of multiple positive Lyapunov exponents in the spectrum, whereas the sheared model produces chaotic orbits only in the neighbourhood of the null point. © *2015 AIP Publishing LLC*. [http://dx.doi.org/10.1063/1.4916402]

I. INTRODUCTION

The spatial location at which the magnitude of a vector field goes to zero is referred to as a *null point*. Null points are useful for studying different topological features.[4,5] The null points of a magnetic field vector are important locations where strong currents can be found.[6] Strong currents play an important role in energy release processes such as magnetic reconnection where a change in the magnetic field topology could release energy to the surrounding plasma. This energy exchange is sometimes accompanied by rapid acceleration of charged particles due to the strong magnetic field-aligned electric fields present (see, for example, Refs. 7–9). Magnetic reconnection near null points has been implicated as the key mechanism behind the observed particle acceleration during various dynamical phenomena in the solar system. In particular, solar flares,[3] plasmoid ejections from the magnetotails of Earth, Jupiter, Saturn, Mercury, and more recently Venus.[10] Examples of magnetic null points have also been reported in the laboratory[11] and in the Earth's magnetosphere.[12] Detection of magnetic null points in numerical experiments requires both a fast and an accurate method.[13]

The first step in understanding charged particle motion in the vicinity of null points was the development of two-dimensional (2D) models and using a test particle approach, on either prescribed electromagnetic fields, i.e., X-type null point configuration[14,15] or fields calculated from the snapshots of magnetohydrodynamics (MHD) simulations.[16] In recent times, three dimensional (3D) models have also been studied in this context. The main features of an isolated 3D magnetic null point are the spine axis and fan plane.[17] The spine axis consists of two oppositely directed isolated field lines which connect at the null point and the fan plane is a continuum of field lines emanating from the null point perpendicular to the spine axis. The test particle approach to 3D geometries has been carried out by Refs. 18–20 using the potential magnetic null point derived by Ref. 17, by investigating the acceleration of charged particles for the spine and fan reconnection scenarios. The test particle approach has also been applied to the electromagnetic fields derived by Refs. 21 and 22 which are solutions to the steady state, resistive, incompressible MHD equations.[23,24] The other 3D null point reconnection regimes developed are the sheared spine/fan and the torsional spine/fan reconnection regimes.[1,2] In the sheared spine/fan case, generic shearing occurs across either the spine axis, fan plane, or both, resulting in a current sheet at the null point which is localised to either the spine, fan plane, or both depending on the location of the shear. In the torsional spine/fan case, field lines in the vicinity of the fan/spine rotate causing current to become concentrated along the spine/fan.

The nonlinear motion of particles around a complex electromagnetic structure provides an interesting example of a dynamical system where chaotic trajectories have been found to exist.[18] Reference 14 performed numerical simulations of the non-relativistic particle motion in an X-type magnetic null configuration and found that particle trajectories in the non-adiabatic region close to the null are chaotic

[a)]a.d.gascoyne@sheffield.ac.uk

in nature and quantified this by calculating a positive value for the maximum Lyapunov exponent.

In this paper, we investigate the motion of a positively charged particle in the vicinity of a 3D magnetic null point for the sheared and torsional spine reconnection scenarios,[1,2] both of which are solutions to the kinematic, steady state, resistive MHD equations. We use a full orbit test particle approach to study the dynamics of a proton injected into the prescribed electromagnetic field. We are interested in whether or not the particle is accelerated in the chosen null point profile. We also deduce the existence of chaotic orbits by calculating the full Lyapunov spectrum.

The paper is structured as follows. In Sec. II, we present the governing equations of particle motion and outline the numerical method used for calculating particle trajectories. Subsections III A and III B are for the sheared and torsional spine magnetic null point profiles, respectively. We describe the model field, where the derivation of the electric field induced by the prescribed magnetic field and discuss the results of various simulated trajectories. In Sec. IV, we investigate the dynamical nature of each system by calculating the complete Lyapunov spectrum for various trajectories. In Sec. V, we give a brief summary and conclusion regarding which model yields accelerated particles and chaotic orbits.

II. GOVERNING EQUATIONS

A set of nonlinear ordinary differential equations describing the motion of a charged particle in the presence of an electric and magnetic field, using Lorentz force $\vec{F} = q(\vec{E} + \vec{v} \times \vec{B})$ and the relativistic momentum defined as $\vec{p} = \gamma m_0 \vec{v}$, are given by

$$\frac{d\vec{x}}{dt} = \frac{\vec{p}}{m_0 \gamma}, \tag{1}$$

$$\frac{d\vec{p}}{dt} = q\left(\vec{E} + \frac{1}{m_0 \gamma}\left[\vec{p} \times \vec{B}\right]\right). \tag{2}$$

Here, t is the time, $\vec{x}$ and $\vec{p}$ are the particle's position and momentum, q and m_0 are its charge and rest mass, and γ is the relativistic (Lorentz) factor. The electric and magnetic fields are represented by $\vec{E}$ and $\vec{B}$, respectively. Solving this set of equations numerically requires rewriting them in a non-dimensional form. Thus, we define

$$X = \frac{x}{L}, \quad Y = \frac{y}{L}, \quad Z = \frac{z}{L}, \quad T = \frac{t}{T_g}, \quad \vec{\rho} = \frac{\vec{p}}{m_0 c},$$
$$\vec{b} = \frac{\vec{B}}{B_0}, \quad \vec{\epsilon} = \frac{\vec{E}}{cB_0}, \quad \mu = \frac{E_0}{cB_0}, \quad \alpha = \frac{T_g c}{L}, \quad q_n = \frac{q}{|q|}, \tag{3}$$

where L and B_0 are the characteristic length scale and field strength, respectively, c is the speed of light, μ_0 is the magnetic permeability, and $T_g = 2\pi m_0/(|q|B_0)$ is the nonrelativistic gyroperiod. Rewriting Eqs. (1) and (2) in dimensionless form using (3), we obtain

$$\frac{d\vec{X}}{dT} = \alpha \frac{\vec{\rho}}{\gamma}, \tag{4}$$

$$\frac{d\vec{\rho}}{dT} = 2\pi q_n \left(\vec{\epsilon} + \frac{1}{\gamma}\left[\vec{\rho} \times \vec{b}\right]\right). \tag{5}$$

We solve the 6th order set of coupled equations (4) and (5) numerically using a 7-step Adams-Bashforth-Moulton (ABM) predictor-corrector scheme. To ensure the stability of the code, we monitor the total energy of the particle during its motion. This quantity should remain constant and is calculated as the sum of kinetic and potential energy,

$$W = K + q\Phi, \tag{6}$$

where we derive Φ from the electric field $\vec{E} = -\vec{\nabla}\Phi$ (see Sec. III for the full explanation of its derivation). The relativistic kinetic energy is calculated by using

$$K = (\gamma - 1)m_0 c^2. \tag{7}$$

We find that the total energy is conserved up to 5 significant figures for the trajectories presented in this paper, demonstrating the validity of our code.

III. MODEL FIELD CONFIGURATIONS

We consider two electromagnetic field configurations which are a solution to the kinematic, steady state, resistive MHD equations near a 3D null point. The first case we shall consider is a sheared case where, the field lines are sheared in the fan plane perpendicular to the spine.[17] The second case we shall consider is a torsional one where the field lines are locally twisted around the spine.[1,2]

A. Case I: Sheared magnetic profile

We consider magnetic field as

$$\vec{B} = \frac{B_0}{L}\left(x, y, -2z + \frac{\mu_0 L}{B_0} J_0 y e^{-4R^2}\right), \tag{8}$$

with null point (0,0,0). Here, $R = \sqrt{(x^2 + y^2)}/L$ and the induced current density is

$$\vec{J} = \frac{1}{\mu_0}\vec{\nabla} \times \vec{B} = J_0\left(1 - 8\frac{y^2}{L^2}, 8\frac{xy}{L^2}, 0\right)e^{-4R^2}. \tag{9}$$

In order to calculate the electric field, we first calculate the electric potential

$$\Phi = -\int \eta \vec{J} \cdot \vec{B} ds, \tag{10}$$

we integrate along the field lines using $ds = \frac{dx}{B_x} = \frac{dy}{B_y} = \frac{dz}{B_z}$, therefore

$$\Phi = -E_0 \frac{x}{R}\frac{\sqrt{\pi}}{4}\mathrm{erf}(2R), \tag{11}$$

where $E_0 = \eta J_0$ is the characteristic electric field strength given in terms of a constant resistivity η. The x and y components of electric field ($\vec{E} = -\vec{\nabla}\Phi$) are thus

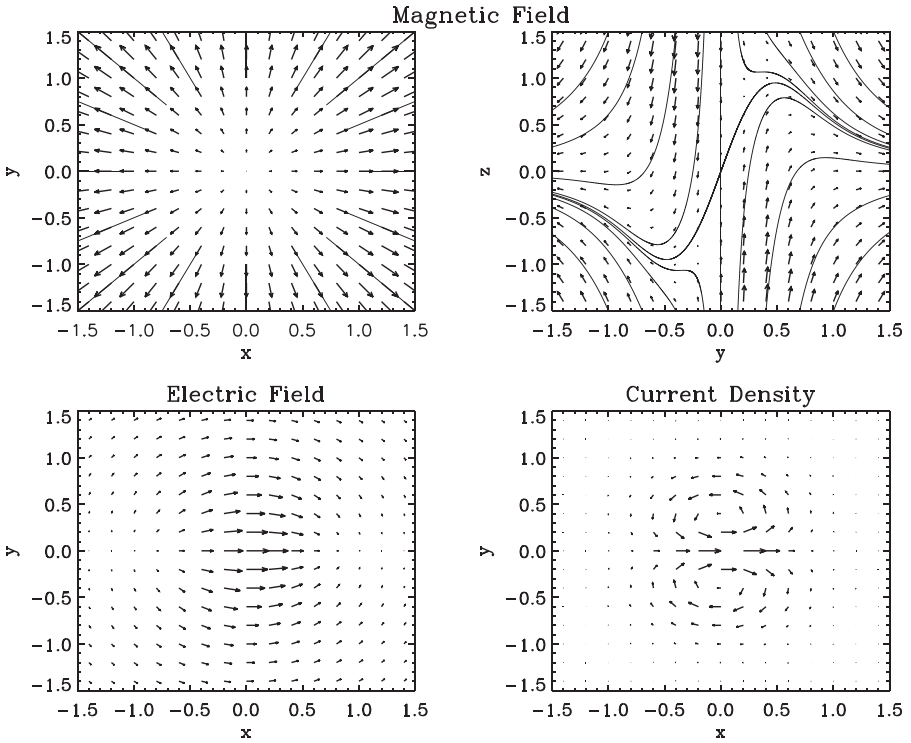

FIG. 1. Top panel: Field plots for the sheared magnetic field profile for $j_0 = 10$. Solid lines correspond to field lines. Bottom panel: The electric field and current density.

$$E_x = E_0 \frac{1}{R^3}\left(\frac{x^2}{L^2} Re^{-4R^2} + \frac{\sqrt{\pi}}{4}\frac{y^2}{L^2}\mathrm{erf}(2R)\right), \tag{12}$$

$$E_y = E_0 \frac{xy}{L^2 R^3}\left(Re^{-4R^2} - \frac{\sqrt{\pi}}{4}\mathrm{erf}(2R)\right), \tag{13}$$

where $\mathrm{erf}(x)$ is the error function and $E_z = 0$. Using (3), the non-dimensional form for the magnetic and electric field can be given by

$$\vec{b} = (X, Y, -2Z + j_0 Y e^{-4R^2}), \tag{14}$$

$$\vec{\epsilon} = \mu_0\left[\frac{1}{R^3}\left(X^2 Re^{-4R^2} + \frac{\sqrt{\pi}}{4}Y^2\mathrm{erf}(2R)\right), \frac{XY}{R^3}\left(Re^{-4R^2} - \frac{\sqrt{\pi}}{4}\mathrm{erf}(2R)\right), 0\right], \tag{15}$$

where $j_0 = (\frac{\mu_0 L}{B_0} J_0)$ is a dimensionless parameter associated with the strength of the current determining to what degree the magnetic field is sheared. By perturbing the fan plane in the vertical direction, this causes a current to be produced in the xy-plane. The magnetic field, electric field, and the current density in x-y plane are shown in Figure 1.

The plasma flow velocity perpendicular to the magnetic field can be obtained by taking the vector product of Ohm's law with $\vec{B}$, which reduces to

$$\vec{v}_\perp = \frac{(\vec{E} - \eta\vec{J}) \times \vec{B}}{B^2}. \tag{16}$$

This is plotted for two different values of j_0 in Figure 2. It can be clearly seen that there are distinct inflow and outflow regions, indicating the possibility of particle acceleration. In the neighbourhood of the null point when the particle distance, as measured from the null-point, becomes comparable to the size of its orbit (Larmor radius in the nonadiabatic region), the adiabatic approximation fails. In this "non adiabatic" region, the particles are freely accelerated by the strong electric field, and the amount of energy gained during its motion is determined by the length of time the particle remains there. For large values of j_0 (increased shear), strong gradients in the magnetic field occur close to the spine axis away from the null point. If the Larmor radius exceeds the length scale of the magnetic field gradient, the adiabatic approximation breaks down and the particle can then be

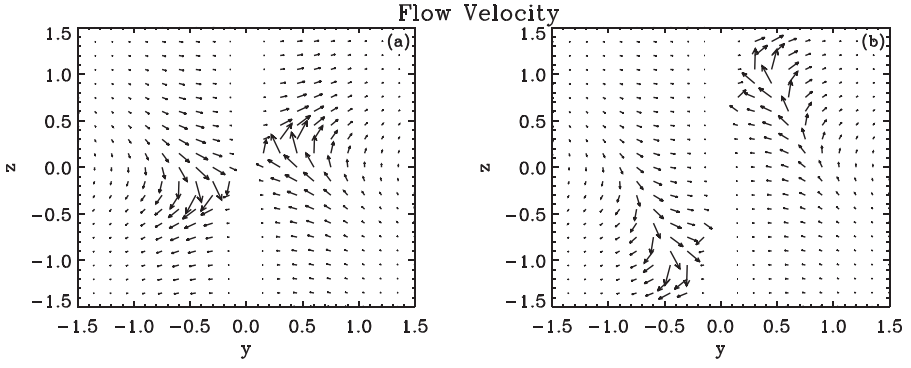

FIG. 2. Field plots for the flow velocity $\vec{v}_\perp$ in the yz-plane for (a) $j_0 = 2$ (weak shear) and (b) $j_0 = 10$ (strong shear).

freely accelerated by the parallel electric field (see Figure 4 for $j_0 = 10$ and $\beta = -70^\circ$).

Proton particle trajectories are calculated for this electromagnetic field configuration by the method mentioned in Sec. II. Input parameters used for the injection of particles, unless stated otherwise, are magnetic field strength $B_0 = 100$ G and scale length $L = 10$ km. The particle is injected into an inflow region in the yz-plane (see the second quadrant in Figure 2) where the electric field is the strongest. The particle's initial position is represented by the parameter β which is the angle with the y-axis on the unit circle centred on the null point. The particle's initial momentum is characterised by an initial energy of 300 eV at a direction represented by the pitch angle, the angle between the initial momentum vector and the magnetic field at the point of injection.

Two regimes are investigated: the weak electric field regime ($E_0 = 100$ V/m) where particle motion is governed primarily by the magnetic field but the particle drifts due to the presence of an electric field albeit weak in strength (see Figure 3). In this case, the particle gains no energy and bounces back and forth between mirror points where the magnetic field converges enough to reflect the particle back to regions of weaker magnetic field strength. The strength of the magnetic shear measured by the value of parameter j_0, only changes the path taken by the particle; the overall dynamics in the weak field regime are essentially the same (i.e., bounce and orbital motion) as shown in Figure 3.

The second and more dynamic regime is the strong electric field regime ($E_0 = 1500$ V/m) shown in Figure 4. Initially, the particle motion is governed by the flow velocity $\vec{v}_\perp$. The particle drifts towards the null point undergo acceleration in the non-adiabatic region and is ejected with sizeable energy gain (Figure 5). After the particle has accelerated away from the null point, its motion is then governed primarily by the magnetic field similar to the weak electric field regime. These two regimes of particle motion were identified by Ref. 15 and further studied by Ref. 18. Particles which travel very close to the null point gain the most energy since they are directly accelerated by the electric field there. The angle of projection β essentially determines how close the particle gets to the null point thus we can find the optimum angle of approach β_{opt} for which particle acceleration is maximum. In Figure 6, we plot β_{opt} as a function of j_0. We find $\beta_{opt} \approx 50^\circ$ for $j_0 = 2$ and $\beta_{opt} \approx 60^\circ$ for $j_0 = 10$. The optimum angle of approach increases initially with magnetic shear before saturating around $j_0 \approx 70^\circ$. For strongly sheared magnetic fields of this type, particles which enter the non-adiabatic region in inflow regions close to the spine will experience the greatest acceleration. The range of β values for which particles reach energy levels $>10^4$ eV for the $j_0 = 2$ weak shear case are $\beta \approx (48^\circ, 55^\circ)$ and for $j_0 = 10$ strong shear case $\beta \approx (57^\circ, 70^\circ)$. Thus, strongly sheared magnetic fields will accelerate a wider range of particles to high energy levels. The particle changes state from being unmagnetised to magnetised after being accelerated, this is evident in the blue and green trajectories where the particle performs the bounce motion. This is the cause of the bumps seen in the kinetic energy plots for these trajectories (Figure 5). As the particle returns toward the null point after being reflected (mirror point close to the fan plane), part of its energy is lost in opposing the electric field and the particle is reflected again (mirror point close to the spine axis) back towards the null point. It gains a small amount of energy back now that

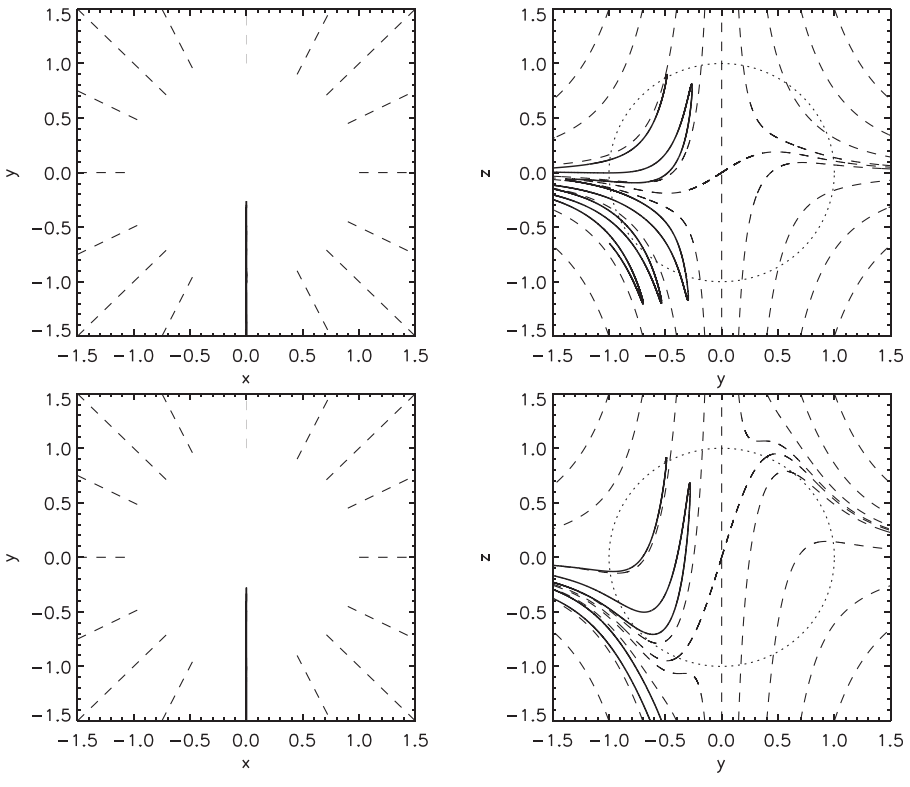

FIG. 3. Particle trajectories for the weak electric field regime $E_0 = 100$ V/m. The initial position of the particle on the unit circle with angle $\beta = -60^\circ$ with the horizontal axis, initial pitch angle 100°, $j_0 = 2$ (top panel) and $j_0 = 10$ (bottom panel). Dashed lines are the magnetic field lines.

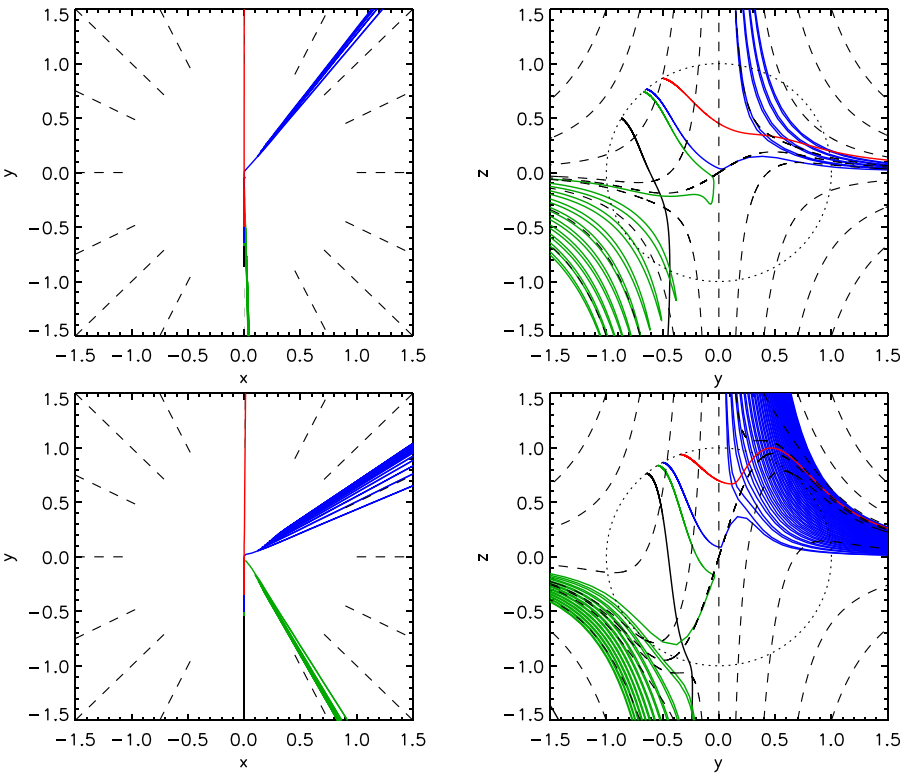

FIG. 4. Particle trajectories for $E_0 = 1500\,\mathrm{V/m}$, initial pitch angle 90° and $j_0 = 2$ and 10, respectively. Initial position on the unit circle $\beta = -[30°, 48°, 50°, 60°]$ (top panel) and $\beta = -[50°, 57°, 60°, 70°]$ (bottom panel).

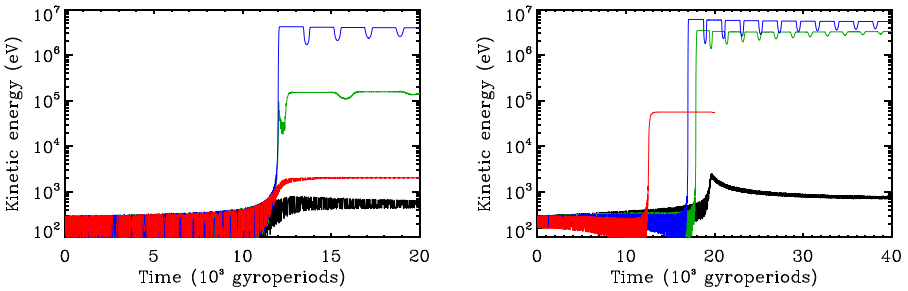

FIG. 5. Kinetic energy vs time for trajectories in Figure 4. Left and right panels correspond to $j_0 = 2$ and $j_0 = 10$, respectively.

the electric field is in the same direction of the particles trajectory. This process occurs several times with continually less effect until the particle is out range of the strong electric field near the null point.

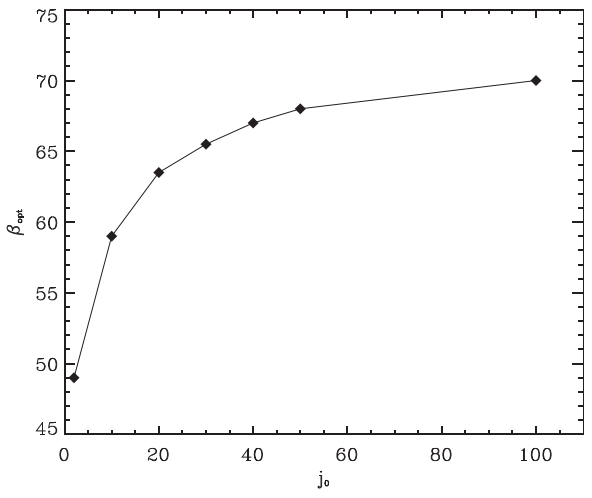

FIG. 6. Optimum angle of approach β_{opt} (for which particle acceleration is maximum) as a function of shear strength j_0.

B. Case II: Torsional spine magnetic profile

The second profile we consider is a torsional spine 3D magnetic null configuration described by the following equation:[2]

$$\vec{B} = \frac{B_0}{L}\left(x - \frac{\mu_0 L}{B_0} J_0 y R^3 e^{-4R^2 - bz^2R^4/L^2}, \right.$$
$$\left. y + \frac{\mu_0 L}{B_0} J_0 x R^3 e^{-4R^2 - bz^2R^4/L^2}, -2z\right), \qquad (17)$$

where b is a dimensionless parameter which localises the twist in height; increasing b localises the twist closer to the fan plane. A value of $b = 0$ causes the twist to be unbounded along the spine (see Figure 7). Using (3) the magnetic field has the following non-dimensional form:

$$\vec{b} = (X - j_0 Y R^3 e^{-Z_R}, Y + j_0 X R^3 e^{-Z_R}, -2Z), \qquad (18)$$

where $Z_R = 4R^2 + bZ^2R^4$. The current density and electric potential are calculated in the same manner as in Sec. III A. The electric potential in non-dimensional form is given by

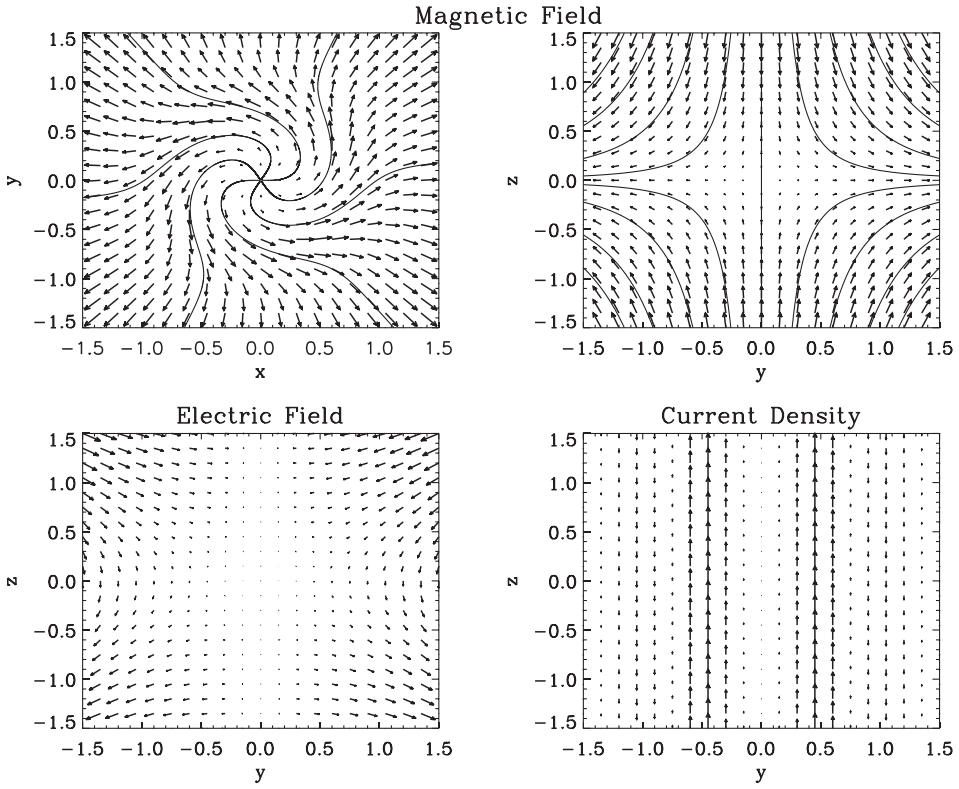

FIG. 7. Field plots for the torsional spine magnetic profile for $j_0 = 40$ and $b = 0$. Solid lines in the top panels correspond to field lines.

$$\Phi = \mu\left[\left(\frac{R^4 b}{4} + \frac{5}{32}R^2 b + \frac{15}{256}b + 2\right)ZR^3 e^{-Z_R} + \left(4 - 4bZ^2R^4 - \frac{15}{512}b\right)\sqrt{\frac{\pi}{4}}\,\mathrm{erf}\left(\sqrt{a}R\right)ZR^2 e^{-bZ^2R^4}\right]. \tag{19}$$

This magnetic field configuration generates a vast different electric field to case I, the key difference being that the electric field is zero at the null point (see Figure 7). The electric field is lot more confined to specific bands and is very irregular for larger values of b (see Figure 8 for $b = 10$).

The perpendicular plasma flow velocity $\vec{v}_\perp$ is obtained using Eq. (16). Figure 9 shows the plots. For $b = 0$ (unbounded twist), the flow is symmetric in the y and z axes but the absence of inflow regions near the null point, means that the particles will not drift towards the null point. This is also true for $b = 10$ (localised twist) but for this case the direction of the plasma flow flips in specific bands above and below the fan plane as shown in right panel of Figure 9. The flow in the xy-plane (not shown here) consists of a spiralling clockwise motion about and away from the spine. This spiralling motion changes direction at certain radii from the spine corresponding to the bands, above and below the fan plane for $b = 10$.

Particle trajectories are calculated in the same manner as Sec. III A with the same input parameters, except that the angle β now relates to the unit circle in the xy-plane, thus β is the angle with the x-axis; $\beta = 60^\circ$ throughout this section and the unit circle is centred at $(0,0,z)$. Once again two regimes of particle motion are again investigated: in the weak field regime ($E_0 = 100$ V/m, Figure 10) behaviour of the particle is similar as in the sheared case but due to the torsional geometry and consequentially the bulk velocities in bands the particle traces out an aesthetically very interesting. This path is due to several factors, the main contributors being: the bounce motion due to the increasing field strength with radius and the clockwise plasma flow in the xy-plane induced by this field geometry. One mirror point occurs on the fan plane a significant distance from the null point and the other occurs along the spine above or below the null

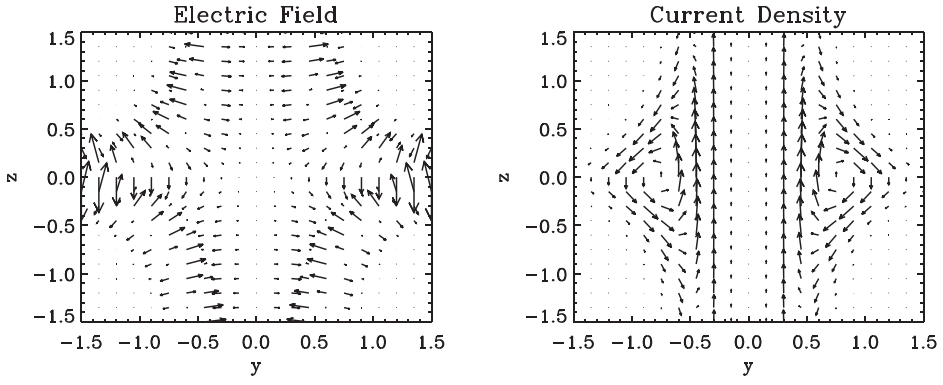

FIG. 8. Electric and current density field plots for the torsional spine magnetic profile for $j_0 = 40$ and $b = 10$.

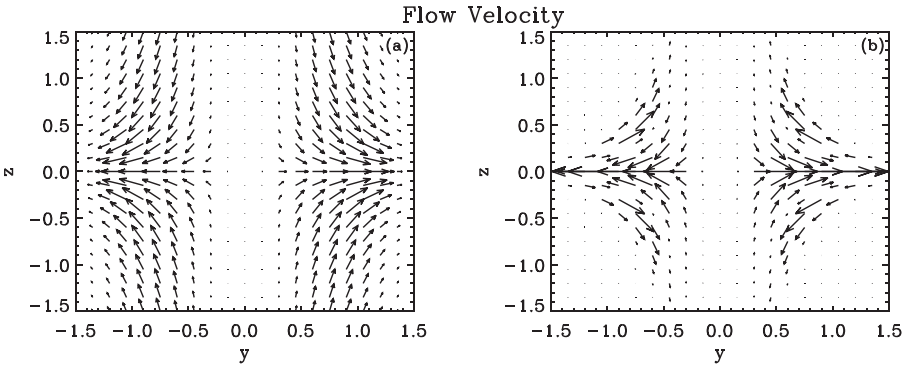

FIG. 9. Field plots for the flow velocity $\vec{v}_\perp$ in the yz-plane for $j_0 = 40$ and (a) $b = 0$ (unbounded twist) and (b) $b = 10$ (local twist).

point depending on initial conditions. Localising the twist close to the fan plane changes the structure of the trajectory but the overall particle motion is essentially the same. The particle undergoes no acceleration in this regime which is expected since the electric field is weak.

Moving to the strong electric field regime ($E_0 = 1500$ V/m), the dynamics change, as expected, with the plasma flow velocity dominates the particles motion. For particles with initial position on or above, the fan plane trajectories spiral radially outward tending to the fan plane. This holds true for both $b = 0$ (unbounded twist) and $b = 10$ (localised twist) (Figure 11). For particles with initial position below the fan plane for the $b = 0$ case, the trajectory exhibits an oscillating motion similar to bounce motions as discussed previously, whilst drifting clockwise around the spine. This bounce motion is due to the opposing flow velocity and electric field in the yz-plane below $z = 0$ (Figures 9(a) and 7, respectively), as opposed to the reflection between mirror points due to the magnetic field as previously seen. The effect of this bounce motion can be seen in the kinetic energy fluctuation of the particle with time, which is very much periodic (Figure 12). For the $b = 10$ case, this bounce motion below $z = 0$ ceases to exist due to the localised and sporadic electric field, instead the particle simply leaves the null point region tending toward the spine. The torsional magnetic geometry produces particle trajectories which are unlikely to be efficient particle accelerators since the particles do not drift toward the null point. The kinetic energy gain seen (Figure 12) is due to the initial position of the particle rather than due to the particle drifting towards the null point which is the case for the sheared magnetic geometry (Sec. III A).

IV. CHAOTIC BEHAVIOUR

The particle trajectories investigated here contain a very distinct structure similar to the various classical dynamical systems (Lorenz, Rossler, etc.). Chaotic orbits have been found to exist in the study of magnetic null geometries, namely, in the work by Refs. 14 and 18. Thus, it would be prudent to investigate whether any chaotic orbits exist in our chosen dynamical systems. We define chaotic orbits in our

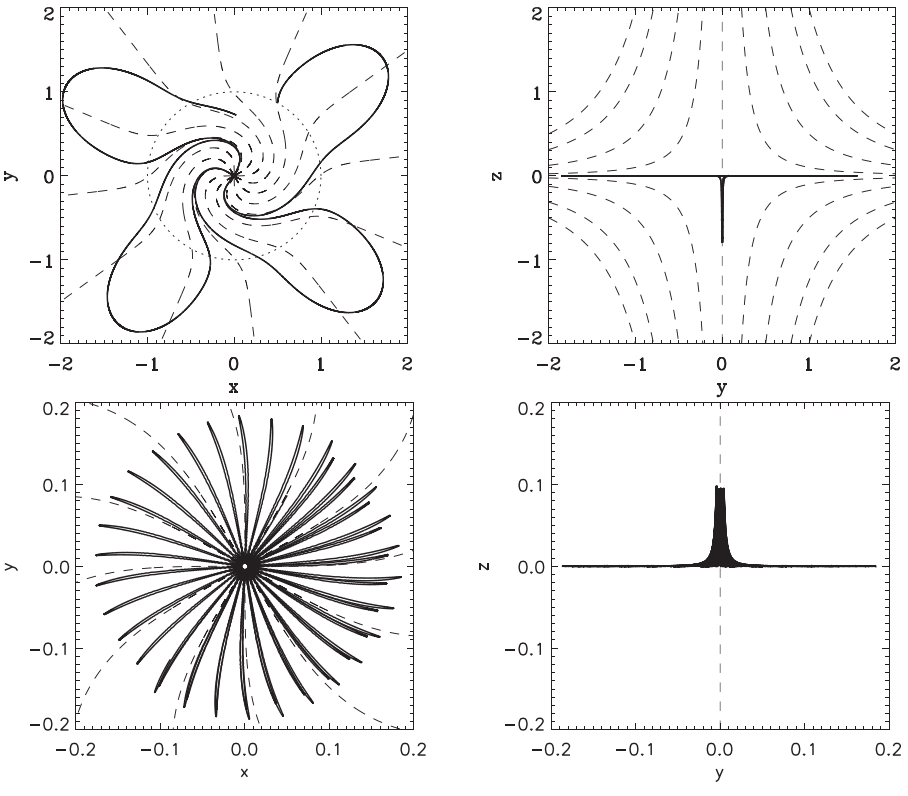

FIG. 10. Particle trajectories for the weak electric field regime $E_0 = 100$, initial pitch angle 130°, initial position $z = 0$, on the unit circle $\beta = 60°$, with current $j_0 = 40$, $b = 0$ (top panel) and $b = 10$ (bottom panel).

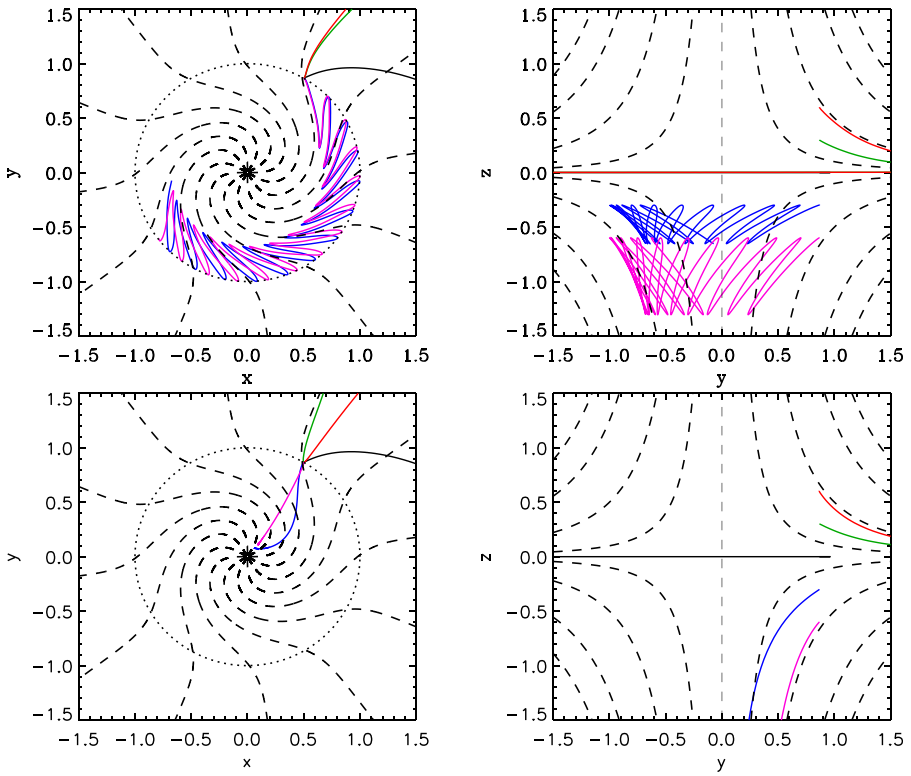

FIG. 11. Particle trajectories for $E_0 = 1500$ V/m, initial pitch angle 130° and $j_0 = 40$. Initial position on the unit circle $\beta = 60°$ for $z = [0,\ 0.3(\text{green}),\ 0.6(\text{red}),\ -0.3(\text{blue}),\ -0.6(\text{magenta})]$, respectively. Top and bottom panels correspond to $b = 0$ (unbounded twist) and $b = 10$ (localised twist), respectively.

context as; infinitesimal differences in initial conditions yield widely diverging orbits. We determine the presences of chaotic orbits with the calculation of positive Lyapunov exponents in its spectrum.

A. Calculating the complete Lyapunov spectrum

One of the common methods to quantify chaotic behaviour of a system's dynamics is to calculate the Lyapunov characteristic exponents (LCEs). Lyapunov exponents measure the separation in time of two orbits starting from arbitrary close initial points. If we regard this small initial separation as a hypersphere of initial points in phase space, and evolve this set through time the dynamics of the system will causes the axes to expand and contract in different directions. The average exponential expansion and contraction rate of each axis are measured by the complete spectrum of Lyapunov exponents. To calculate the full spectrum of LCEs for the two dynamical systems investigated (sheared and torsional spine), we adopt the algorithm discussed in Refs. 25–27.

The 6-dimensional autonomous smooth dynamical system defined by Eqs. (4) and (5) can be written in the generalised form

$$\dot{\vec{x}} = \vec{F}(\vec{x}). \tag{20}$$

Suppose (20) has a solution $\vec{f}_t(\vec{x})$, thus satisfies $\vec{F}(\vec{f}_t(\vec{x})) = \dot{\vec{f}}_t(\vec{x})$. Given the initial condition $\vec{x}_0$ we have $\vec{f}_t(\vec{x}_0)$, where $\vec{f}_0(\vec{x}_0) = \vec{x}_0$ thus the set $[\vec{f}_t(\vec{x}_0) : t \in \mathbb{R}]$ is a trajectory of the system with starting point $\vec{x}_0$ and time t. If we consider a small perturbation $\vec{u}_0$ thus obtaining two nearby points $\vec{x}_0$ and $\vec{x}_0 + \vec{u}_0$ there respective trajectories after some time are $\vec{f}_t(\vec{x}_0)$ and $\vec{f}_t(\vec{x}_0 + \vec{u}_0)$ giving there new separation as

$$\vec{u}_t = \vec{f}_t(\vec{x}_0 + \vec{u}_0) - \vec{f}_t(\vec{x}_0) = D_{\vec{x}_0}\vec{f}_t(\vec{x}_0) \cdot \vec{u}_0, \tag{21}$$

where $D_{\vec{x}_0}$ is the derivative with respect to $\vec{x}_0$ thus the last term is obtained by linearising $\vec{f}_t$. Therefore, the Lyapunov exponent for the expansion of the two trajectories is defined as

$$\lambda(\vec{x}_0, \vec{u}_0) = \lim_{t\to\infty} \frac{1}{t} \ln \frac{||\vec{u}_t||}{||\vec{u}_0||} = \lim_{t\to\infty} \frac{1}{t} \ln ||D_{\vec{x}_0}\vec{f}_t(\vec{x}_0)||, \tag{22}$$

where $||\cdot||$ is defined as the Euclidean norm. Equation (22) provides us with only one LCE since we have only

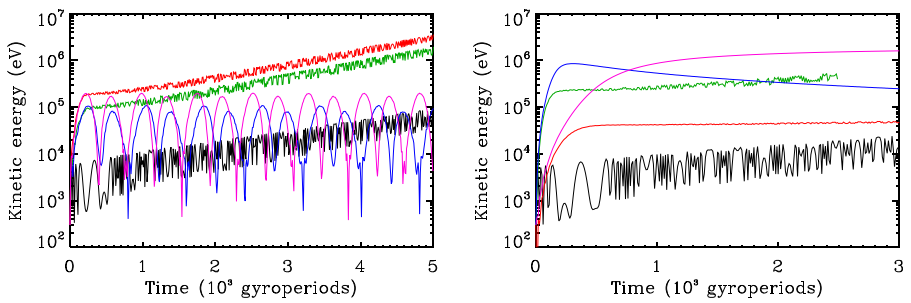

FIG. 12. Kinetic energy vs time for trajectories in Figure 11. Left and right panels correspond to $b = 0$ and $b = 10$, respectively.

considered a single tangent vector $\vec{u}_0$. We can extend this definition by considering the LCEs of order 6 which describe the mean rate of growth of a 6-dimensional volume i.e., a parallelepiped whose edges correspond to the set of 6 linearly independent vectors $\mathbf{U}_0 = [\vec{u}_1, \ldots, \vec{u}_6]$, thus the LCEs of order 6

$$\lambda^6(\vec{x}_0, \mathbf{U}_0) = \lim_{t\to\infty} \frac{1}{t} \ln[\mathrm{Vol}^6(D_{\vec{x}} \vec{f}_t(\mathbf{U}_0))], \tag{23}$$

where Vol^6 is the 6-dimensional volume of the parallelepiped. Equation (23) can be expanded to obtain[27] in descending order

$$\lambda^6(\vec{x}_0, \mathbf{U}_0) = \lambda(\vec{x}, \vec{u}_1) + \cdots + \lambda(\vec{x}, \vec{u}_6), \tag{24}$$

we define $\lambda_1 = \lambda(\vec{x}, \vec{u}_1)$ etc. Since the dynamical system concerned here is conservative it is a measure-preserving flow and thus $\sum_{i=1}^{6} \lambda_i = 0$. Summarising, we calculate the "fiducial" trajectory (centre of the volume) by the action of the set of nonlinear equations on the initial condition x_0. The trajectory of the volume is calculated by the action of the linearised set of equations on the initial vectors $\mathbf{U}_0$ which are anchored infinitesimally close to x_0 (see Eq. (21)). The linearised set of equations take the following form:

$$\dot{\mathbf{U}}_t = \mathcal{J} \cdot \mathbf{U}_t, \tag{25}$$

where $\mathcal{J}$ is the Jacobian matrix of the nonlinear system (20). The spectral calculation of the Lyapunov exponents requires the integration of the nonlinear system of 6 equations, (20), together with the integration of the linearised system of 36 equations, (25). Such a calculation has a tendency to align the axes ($\mathbf{U}_t$) in the direction of the most rapid growth thus no longer maintaining there orthonormality, resulting in only calculating the largest LCE.[26] This problem can be overcome by repeatedly applying the Gram-Schmidt reorthonormalisation (GSR) procedure on the vector frame $\mathbf{U}_t = [\vec{u}_1, \ldots, \vec{u}_6]$ at time t,

$$\begin{aligned}
\vec{w}_1 &= \vec{u}_1, & \vec{v}_1 &= \frac{\vec{w}_1}{||\vec{w}_1||},\\
\vec{w}_2 &= \vec{u}_2 - \langle \vec{u}_2, \vec{v}_1 \rangle \vec{v}_1, & \vec{v}_2 &= \frac{\vec{w}_2}{||\vec{w}_2||},\\
&\vdots & &\vdots\\
\vec{w}_6 &= \vec{u}_6 - \sum_{i=1}^{5} \langle \vec{u}_6, \vec{v}_i \rangle \vec{v}_i, & \vec{v}_6 &= \frac{\vec{w}_6}{||\vec{w}_6||},
\end{aligned} \tag{26}$$

where $\langle \cdot \rangle$ signifies the inner product. The GSR procedure provides us with the orthonormal set $\mathbf{V}_t = [\vec{v}_1, \ldots, \vec{v}_6]$. It is clear that the orientation of the first vector $\vec{u}_1$ is unchanged by GSR and thus seeks out the direction in tangent space which is most rapidly growing. It follows from (26) that the volume of the 6-dimensional parallelepiped spanned by $\mathbf{U}_t$ satisfies

$$\mathrm{Vol}^6[\vec{u}_1, \ldots, \vec{u}_6] = ||\vec{w}_1|| \cdots ||\vec{w}_6||. \tag{27}$$

The 6th order LCEs (23) can be rewritten to obtain for the sth step

$$\lambda^6(\vec{x}_0, \mathbf{U}_0) = \lim_{s\to\infty} \frac{1}{s\delta h} \sum_{i=1}^{s} \ln(||\vec{w}_1|| \cdots ||\vec{w}_6||)_i, \tag{28}$$

where δh denotes the step size and $(||\vec{w}_1|| \cdots ||\vec{w}_6||)_i$ denotes the set of orthogonal vectors calculated at the ith step. Each individual exponent can be continually calculated for a suitable value of δh as

$$\frac{1}{s\delta h} \sum_{i=1}^{s} \ln(||\vec{w}_1||)_i \approx \lambda_1, \ldots, \frac{1}{s\delta h} \sum_{i=1}^{s} \ln(||\vec{w}_6||)_i \approx \lambda_6. \tag{29}$$

Table I contains the numerically calculated Lyapunov spectrum for the sheared and torsional magnetic profiles investigated in this paper. We find that in the weak electric field regime in both profiles produce periodic orbits which are not chaotic since each exponent is approximately zero. In the strong electric field regime, the sheared model produces

TABLE I. Lyapunov spectrum for the two dynamical systems studied for various initial parameters as computed numerically using the method outlined in Sec. IV A.

System	Parameter values	Lyapunov spectrum
Sheared magnetic field	Figure 3 trajectories	$\lambda_1 = 0,\ \lambda_4 = 0$
	$E_0 = 100$ V/m	$\lambda_2 = 0,\ \lambda_5 = 0$
	$j_0 = 2{,}10$	$\lambda_3 = 0,\ \lambda_6 = 0$
	Figure 13, trajectory	$\lambda_1 = 0.05,\ \lambda_4 = -0.0028$
	$E_0 = 1500$ V/m	$\lambda_2 = 0.005,\ \lambda_5 = -0.0226$
	$j_0 = 10$	$\lambda_3 = -0.001,\ \lambda_6 = -0.0287$
Torsional magnetic field	Figure 10, trajectories	$\lambda_1 = 0,\ \lambda_4 = 0$
	$E_0 = 100$ V/m	$\lambda_2 = 0,\ \lambda_5 = 0$
	$b = 0{,}10$	$\lambda_3 = 0,\ \lambda_6 = 0$
	Figure 11, trajectory	$\lambda_1 = 0.2846,\ \lambda_4 = 0.0049$
	$E_0 = 1500$ V/m	$\lambda_2 = 0.109,\ \lambda_5 = -0.1133$
	$b = 0$	$\lambda_3 = 0.0021,\ \lambda_6 = -0.2874$
	Figure 11, trajectory	$\lambda_1 = 0.2675,\ \lambda_4 = -0.0074$
	$E_0 = 1500$ V/m	$\lambda_2 = 0.1089,\ \lambda_5 = -0.0975$
	$b = 0$	$\lambda_3 = 0.0386,\ \lambda_6 = 0.31$

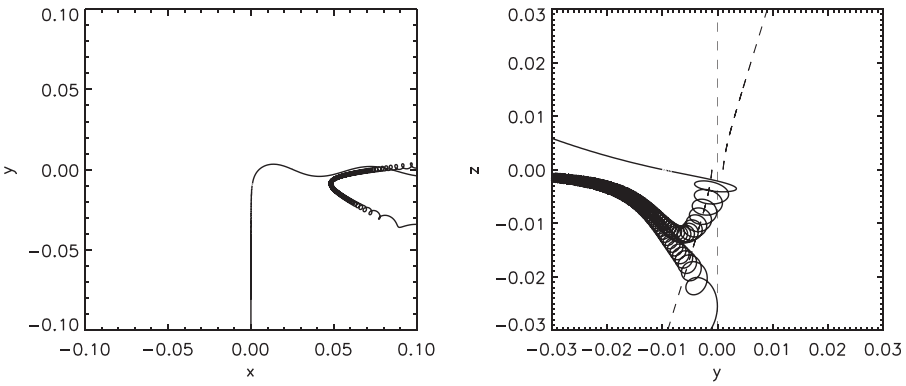

FIG. 13. Particle trajectory for the sheared magnetic null profile for $E_0 = 1500\,\mathrm{V/m}$, initial pitch angle $90°$, $j_0 = 10$ and $\beta = 58.9°$. Dashed lines represent the magnetic field. Note also the small scales on the axis.

weak hyperchaotic trajectories if the particle approaches the null point very closely (as in Figure 13). We define hyperchaotic orbits as having two or more positive Lyapunov exponents.[26] The torsional model produces hyperchaotic orbits for particles with initial position off the fan plane. This suggests the chaotic orbits exist if the particle propagates into regions of strong electric field since the orbits are not chaotic in weak or zero electric field regions (fan plane for the torsional model and anywhere away from the spine for the sheared model). Since both the models obey the conservation of energy, they are measure preserving flows. Thus, the sum of the Lyapunov exponents should be zero as discussed earlier. From Table I, we see that this is indeed the case.

V. CONCLUSION

We investigated the dynamics of particle motion in a new class of electromagnetic field configurations, namely, the sheared and torsional spine reconnection scenarios which are solutions to the kinematic, steady state, resistive MHD equations at a 3D null point. The particle trajectories were calculated by using a numerical code which solved the 6th order set of nonlinear ordinary differential equations describing the motion of a particle under the influence of a magnetic and electric field. The method applied to solve the governing equations is the 7-step ABM predictor corrector scheme (see Sec. II).

We found that the two model magnetic fields produced very different electric fields and as a consequence very different plasma flows $\vec{v}_\perp$ perpendicular to the magnetic field. The sheared model produced plasma flows with well defined inflow and outflow regions. Such magnetic configuration may be a possible particle accelerator; significant particle acceleration occurs for particles which drift into the non-adiabatic region close to the null point and the particle is freely accelerated by the strong electric field located there. The parameter j_0 controlled the amount of shear across the fan plane and we found that for increased shear the optimum angle of approach occurs at higher latitudes and the range of accelerated particles also increases. On the other hand, particle acceleration in the torsional case looked unlikely due to the flows being mainly outward (Figure 9). Although for the $b = 0$ case of unbounded twist, the particles with initial position below the fan plane exhibit a bounce motion whilst orbiting the spine due to the opposing electric and flow field (Figure 11). For most initial positions and model parameters, the particles simply follow the bulk velocity moving away from the null point.

We carried out further investigations to truly confirm the existence of chaotic orbits. We calculated the full spectrum of Lyapunov characteristic exponents which measure the average exponential rate of divergence or convergence of orbits starting from nearby initial conditions. We found that for the sheared model the chaotic orbits exist only for trajectories that are close to the null point; however, the nearby trajectories diverge slowly as suggested by the very small, largest Lyapunov exponent (see Table I). The torsional model on the other hand produces hyperchaotic orbits in the strong electric field regime for particles with initial conditions not on the fan plane. This is evident from multiple positive Lyapunov exponents. The main conclusion from this study is that although the sheared magnetic field model is the most promising particle accelerator, the torsional magnetic field model is far more interesting dynamically due to the highly chaotic nature of particle motions in this configuration.

ACKNOWLEDGMENTS

The author would like to thank R. Jain for the help in preparation of this manuscript and for useful discussions. The author also gratefully acknowledges useful discussions with P. Wyper and support from STFC (UK).

[1]E. R. Priest and D. I. Pontin, Phys. Plasmas **16**, 122101 (2009).
[2]P. Wyper and R. Jain, Phys. Plasmas **17**, 092902 (2010).
[3]R. P. Lin, Space Sci. Rev. **124**, 233 (2006).
[4]T. N. Bungey, V. S. Titov, and E. R. Priest, Astron. Astrophys. **308**, 233 (1996).
[5]C. J. Schrijver and A. M. Title, Sol. Phys. **207**, 223 (2002).
[6]S. I. Syrovatskii, Annu. Rev. Astron. Astrophys. **19**, 163 (1981).
[7]P. Goldreich and W. H. Julian, Astrophys. J. **157**, 869 (1969).
[8]M. A. Ruderman and P. G. Sutherland, Astrophys. J. **196**, 51 (1975).
[9]Y. E. Litvinenko, Astrophys. J. **462**, 997 (1996).
[10]T. L. Zhang, Q. M. Lu, W. Baumjohann, C. T. Russell, A. Fedorov, S. Barabash, A. J. Coates, A. M. Du, J. B. Cao, R. Nakamura, W. L. Teh, R. S. Wang, X. K. Dou, S. Wang, K. H. Glassmeier, H. U. Auster, and M. Balikhin, Science **336**, 567 (2012).
[11]R. L. Stenzel, J. M. Urrutia, M. Griskey, and K. Strohmaier, Phys. Plasmas **9**, 1925 (2002).
[12]C. J. Xiao, X. G. Wang, Z. Y. Pu, H. Zhao, J. X. Wang, Z. W. Ma, S. Y. Fu, M. G. Kivelson, Z. X. Liu, Q. G. Zong, K. H. Glassmeier, A. Balogh, A. Korth, H. Reme, and C. P. Escoubet, Nat. Phys. **2**, 478 (2006).
[13]A. L. Haynes and C. E. Parnell, Phys. Plasmas **14**, 082107 (2007).
[14]L. Nocera, F. Pegoraro, S. V. Bulanov, and G. Bertin, Phys. Scr. **63**, 197 (1996).
[15]G. E. Vekstein and P. K. Browning, Phys. Plasmas **4**, 2261 (1997).

[16]M. Gordovskyy, P. K. Browning, and G. E. Vekstein, Astron. Astrophys. **519**, A21 (2010).
[17]E. R. Priest and V. S. Titov, Philos. Trans. R. Soc. London **354**, 2951 (1996).
[18]S. Dalla and P. K. Browning, Astron. Astrophys. **436**, 1103 (2005).
[19]S. Dalla and P. K. Browning, Astrophys. J. **640**, L99 (2006).
[20]S. Dalla and P. K. Browning, Astron. Astrophys. **491**, 289 (2008).
[21]I. J. D. Craig, R. B. Fabling, S. M. Henton, and G. J. Rickard, Astrophys. J. **455**, L197 (1995).
[22]I. J. D. Craig and R. B. Fabling, Astrophys. J. **462**, 969 (1996).
[23]Y. E. Litvinenko, Astron. Astrophys. **452**, 1069 (2006).
[24]A. Stanier, P. Browning, and S. Dalla, Astron. Astrophys. **542**, A47 (2012).
[25]G. Benettin, L. Galgani, A. Giorgilli, and J. M. Strelcyn, Meccanica **15**, 9 (1980).
[26]A. Wolf, J. B. Swift, H. L. Swinney, and J. A. Vastano, Physica D **16**, 285 (1985).
[27]M. Sandri, Math. J. **6**, 78 (1996).